An Integrated Statistical Approach for Volume Reconstruction from Unregistered Sequential Slices

Yong Yu[1], **Alain Trouvé**[1], **Jiaping Wang**[2] **and Bernard Chalmond**[1]

[1] CMLA, ENS Cachan, CNRS, UniverSud, 61 Avenue Président Wilson, 94230 Cachan cedex France

[2] LAGA/L2TI, Institut Galilée, Université Paris XIII, 99 avenue J.B. Clément, 93430 Villetaneuse, France

E-mail: [1]{yu, trouve, Bernard.chalmond}@cmla.ens-cachan.fr, [2]wang@math.univ-paris13.fr

Abstract.

We address the problem of volume reconstruction from a sequence of cross-sections in the case where the cross-sections positions are unknown. That implies to perform simultaneously registration and reconstruction. We propose a statistical formulation of the problem leading to an energy minimisation algorithm as well as an automatic calibration procedure for the energy parameters. This method has been developed in the context of micro-rotation confocal microscopy. Experiments in this context illustrate the ability of this method to reconstruct efficiently the object of interest.

PACS numbers: 42.30.Wb, 45.10.Db, 87.57.nj, 87.57.cf, 87.57.cp, 87.64.mk

Submitted to: *Inverse Problems*

1. Introduction

We address the problem of reconstructing a 3-D volume of intensities (3-D image) from a sequence of 2-D cross-section images called slices. To illustrate this problem in a simple context let us see Fig.1 which shows a 2-D reconstruction from a sequence of 1-D cross-sections (profile lines). The initial reconstruction of the 2D image from the badly posed profile lines is of rather low quality, (Fig.1c). The main difficulty in performing the reconstruction is that the position of each slice is unknown. If these positions were known, the problem would be similar to an interpolation/smoothing problem. On the other hand, if the 3-D image was known, the estimation of the position of a particular slice, would reduce to a registration problem. So, we need to couple these two sub-problems in a common formulation which implies performing simultaneously registration (slice positioning in our case) and reconstruction.

The method we propose is generic. It has been designed in [1] while taking into account the specifics of our domain of application, that is, micro-rotation confocal microscopy. We are concerned by 3-D fluorescence imaging of individual living non adherent cells in the goal of multi-dimensional measurements [2], [1]. Several proposals for 3-D cell representation have been presented in recent years but all these techniques need to fix the cell in some orientations and thus, they are limited to adherent cells [3], [4], [5], [6], [7], [8].

Our confocal microscope is equipped with a dielectrophoretic field cage wherein suspended cells can be trapped and then automatically manipulated [9]. Once an individual cell has been trapped, the parameters of the dielectrophoretic field are ruled in order that the cell undergoes continuous rotations around a main axis ‡. During the rotation, a sequence of microscopic images, called micro-rotation images, are sampled at a given rate. Each slice is an image taken under the same microscopic conditions. A first advantage of such an apparatus is the ability to see non adherent living cells under different views without having to manually manipulate them. However, analysing such a 2-D sequence and mentally inferring 3-D structures is not an easy matter (see Fig.2). We need a complete digital 3-D representation of the cell which can allow for inspection and measurement.

In the case of micro-rotation microscopy, the rotation movement (axis and angular velocity) is unstable and corrupted by erratic small translations. More generally, the position of every slice is completely defined by an unknown rigid transformation combining rotation and translation with respect to a coordinate frame. This unstable movement makes slice motion estimation and volume reconstruction a challenging problem. Our results show that this problem is feasible with accuracy, a fact of which we doubted when we have started this research five years ago.

Before going into the specific application, let us mention several fields which at first glance share some features with this problem. In aerial imaging, simultaneous registration-restoration has been studied to achieve super-resolution [10]. In this case, registration deals only with very small two-dimensional translations and the purpose of the treatment is directed more towards fusion than reconstruction. In robotics, Structure From Motion techniques try to

‡ More imaging acquisition detail can be founded in http://www.pfid.org/AUTOMATION/gallery/PEcell1.shtml

compute the external structure of a rigid object from the motion of its geometrical projections onto a 2-D surface [11], but not its internal structure. Although we have not exactly found the same problem in the literature, it is interesting to remark that there are similar problems in the projection tomography domain (e.g. electron microscopy, conventional X-ray imaging systems, etc). The methods to treat these related problems are either based on the matching of projection moments according to the Helgason-Ludwig conditions (see [12, 13] in 2D case and [14] in 3D case), or based on the spatial relationship determination from the common lines shared by any projection pairs in Fourier space thanks to the central section theorem [15, 16].

The performance of common line based methods are however limited by the low SNR measurement of the microscopy imaging systems. The moments based algorithm [13] for 2D tomography needs an initial translation estimation. Translations are first estimated by shifting the center of mass of each projection to the origin. In the case of fluorescence mycroscopy, this approach is not valid since the center mass of each 2D slice is not related to the center of mass of the 3D cell. Furthermore, slices are optical cross sections which are different from a line integration process as in the case of projection tomography. Therefore, we have not found treatment to express the dependence between slice positions and slice measurements or extracted features as done in [13].

Below, slices positioning and volume reconstruction will be driven by spatial constraints on volume coherence through a functional linking position and volume. To measure this coherence between registered slices, a continuous volume model is indispensable which means that alignment and reconstruction are interwoven. Instead of working directly on the common space $\mathbb{L}^2$, we restrict the unknown volume to be in a Hilbert space $\mathcal{H}$ associated with a reproducing kernel. In the work of G. Matheron [17], the equivalence between spline and kriging is well established. Therefore, the a priori model on volume to reconstruct is in fact posed as a Gaussian random process whose covariance function defines the spatial dependency. The regularity of the volume is then maintained during the simultaneous estimation of both volume and slices positions. In Section 2, after stating our problem, a probabilistic framework is introduced to model both the cell volume structure and the slice positions. Volume reconstruction including parameters estimation and slice positioning is performed in an integrated statistical framework. A variational formula is derived in Section 3. To remove the painful trial-and-error process of tuning coefficients of energy terms, an automatic statistical estimation of parameters via maximum likelihood principle is proposed in Section 4. Experimental results are given in Section 5.

2. Problem statement and statistical model description

2.1. Problem statement

A sequence of image slices $I \doteq (I_t)_{1\leq t\leq N}$ is obtained through a fixed plane H_0 intersecting the moving object. In microscopy, H_0 is the focal plane. Fig.2 shows twelve slices acquired in H_0 ($\sim$340 slices per tour) of a cell in rotation. The images are all recorded in a same frame in

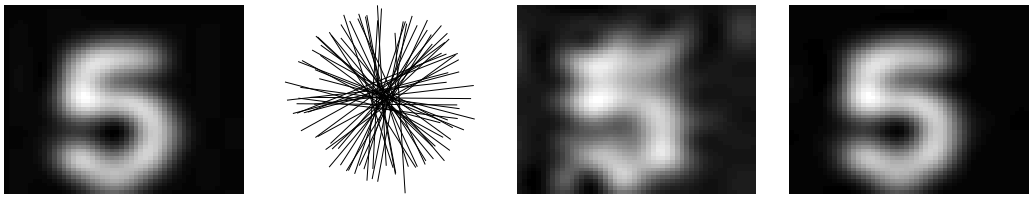

(a) True image f (b) True slice positions $\{\phi_i\}$ (c) Initial reconstruction (d) Fifth and last reconstruction

Figure 1. A 2-D reconstruction example.

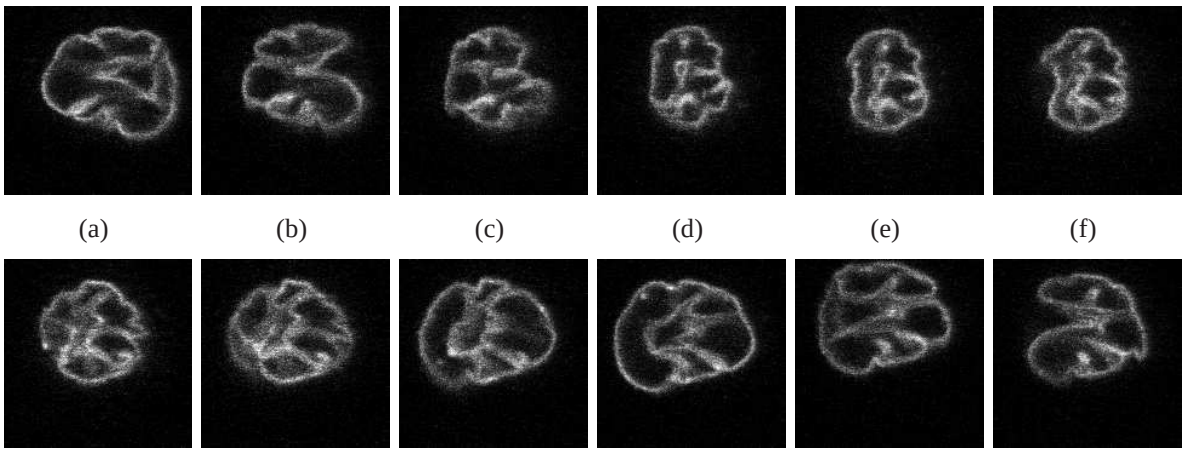

Figure 2. 12 micro-rotation slices from a real confocal microscopy imaging data sequence.

H_0 and consequently their position inside the object is unknown. This situation is equivalent to the situation where the object is fixed and H_0 is moving. For pose estimation, the object is considered as fixed and then for every image slice, we search for the displacement which moves this image from H_0 to its right position inside the object. So, we have to estimate the slice positions represented by N affine transformations $\Phi \doteq (\varphi_i)_{1\leq i\leq N}$ and at the same time, the continuous 3-D image f whose cross-section $f \circ \varphi_i$ at position φ_i is close to the observed image I_i.

As mentioned in Introduction, the difficultly here is that two problems which are well known and have already been intensively explored are compounded. If the affine parameters Φ were fixed, the reconstruction of f would be an interpolation/smoothing problem from irregular data (see [18] and the references therein). On the other hand, if the true volume f was known, to find the true position of each slice would be a rigid registration problem as solved in [5]. We propose a statistic model for both volume reconstruction and slice positioning; this yields a variational approach based on a posterior joint probability density of Φ and f.

2.2. Statistical modeling

We assume that the movement of the object corresponds to a random perturbation around a mean movement Φ^0. We suppose also that Φ^0 is given or can be estimated as it is the case in micro-rotation microscopy. Now, given the data set $\{I_i\}$, the task is to estimate the transformations Φ more accurately in such a way that $f \circ \Phi \approx I$, and at the same time to reconstruct the volume f. Classically, this problem can be formalized in the framework of "inverse problems" [19]. The basic idea is to define an a-priori model for the pair (f, Φ) and to estimate (f, Φ) by Bayesian inference. Here this consists of choosing the solution $(\hat{f}, \hat{\Phi})$ that maximizes the a-posteriori probability (MAP criterion):

$$\begin{aligned}(\hat{f}, \hat{\Phi}) &= \text{argmax}_{f,\Phi} P(f, \Phi | I) \\ &= \text{argmax}_{f,\Phi} \frac{P(I|f, \Phi)P(f)P(\Phi)}{P(I)} \ . \end{aligned} \tag{1}$$

We now provide general expression of $P(I|f, \Phi)$, $P(f)$ and $P(\Phi)$.

• First, the image I_i is seen as a noisy version of $f \circ \varphi_i$, with some additive noise:

$$I_i(x) = f \circ \varphi_i(x) + \epsilon_i(x) \ , \quad \forall x \in H_0 \ . \tag{2}$$

We assume that differences $\{\epsilon_i(x) \ x \in H_0\}$ are independently and identically distributed according to the Gaussian law $\mathcal{N}(0, \sigma_\epsilon^2)$, and consequently the probability distribution of I_i given (f, φ_i) is

$$P(I_i|f, \varphi_i) \propto \exp(-\sum_x |I_i(x) - f(\varphi_i(x))|^2 / \sigma_\epsilon^2) \ . \tag{3}$$

Furthermore, we assume that slices $\{I_i\}$ are conditionally independent given (f, φ) which implies

$$P(I|f, \Phi) = \prod_{i=1}^{N} P(I_i|f, \varphi_i) \ .$$

• Second, we have to define a prior on f. In our context, this definition is crucial since the role of the prior is to insure smooth reconstruction by interpolating sparse and non organized points and also by this way to quantify the regularity of the volume. For non organized points smoothing, a well know approach is the "kriging" technique [20, 21] which can be efficiently rewritten using a Reproducing Kernel Hilbert Space $\mathcal{H}$ (RKHS) formulation [22] (see [23] for the tomography domain). This is quite technical. Briefly, f is represented by a linear combination of N_c elements $k(x_i, \cdot)_{1 \le i \le N_c}$ in $\mathcal{H}$:

$$f(\cdot) = \sum_{1 \le i \le N_c} \alpha_i k(x_i, \cdot) \ , \tag{4}$$

where $k(\cdot, \cdot)$ is a kernel function modeling the spatial dependency within f :

$$k(x, y) = \rho(\|(x - y)\| / \lambda_f) \ . \tag{5}$$

With this definition, the unknown continuous volume f is replaced by the unknown set of parameters (α_i). As in the case of kriging, we have chosen the Gaussian function for ρ. λ_f is a scale parameter which defines the range of the spatial dependency, as a covariance function

does. *The control points (x_i) in (4) are chosen at 3D regularly spaced grid locations covering the region in which the volume reconstruction has to be done. The grid resolution is defined by N_c and is equivalent to the image resolution.* With this definition and the reproducing property of $\mathcal{H}$, that is $\langle k(x_i,.), k(x_j,.)\rangle_{\mathcal{H}} = k(x_i,x_j)$, the norm of f is

$$\|f\|^2_{\mathcal{H}} = \sum_{i,j} \alpha_i \alpha_j k(x_i,x_j) \ .$$

Finally we define the Gaussian prior on f by

$$P(f) \propto \exp(-\frac{\|f\|^2_{\mathcal{H}}}{2\sigma_f^2}) \ , \tag{6}$$

where σ_f^2 is a regularization parameter which tunes the amplitude of the variations of f. Greater is the probability, and greater is the regularity of f with respect to the kernel k.

In summary, the role of this model is to quantify the regularity of the volume through Gaussian structure, and also to treat the interpolation/smoothing task, a difficult task since here the data are badly distributed : in the case of object in rotation, many data points are present around the rotation center whereas far from this center, data points are very sparse. *Let us note that the simple $\mathbb{L}^2$ norm $\|f\|$ as in [24], would not be suitable. In short, (1) leads to minimize in f (when the ϕ_i's are fixed) the energy $E(f) \doteq \sum_{i=1}^N \sum_{x\in H_0} |I_i(x) - f\circ\varphi_i(x)|^2 + \gamma\|f\|^2$ where $\gamma = \sigma_\epsilon^2/\sigma_f^2$. Since there is no data between slices, the minimizer $\hat{f}$ of this function tends to be abnormally small at these locations. Note more importantly that the energy E is actually not defined on the $\mathbb{L}^2$ space since data term is depending only on the values on f on a negligeable set for the 3D Lebesgue measure . Of course, a non degenerated solution could be obtained if we restrict the optimization to a finite dimensional subpace of $\mathbb{L}^2$ as given by the parametric formulation of (4). However, the dimensionality N_c of this subpace will then be a regularization parameter to be estimated in addition to the scale λ_f. In constrast, the natural RKHS norm associated with the kernel k is stable for increasing N_c values provided that the sampling is fine enough with respect to the scale λ_f. Morever, the use of the RKHS norm is mandatory to make the proper link with the statistical framework we are developing hereafter for the estimation of parameters.*

In this way, many papers have demonstrated the necessity to introduce prior spatial dependency in tomographic reconstruction ([25, 26] among many others).

• Third, for the prior $P(\Phi)$, we assume that the φ_i's are independent isotropic perturbations of the mean positions φ_i^0, that is:

$$P(\Phi) \doteq P_{\Phi^0}(\Phi) = \prod_{i=1}^N P_{\varphi_i^0}(\varphi_i) \ .$$

Models based on more sophisticated assumption could be designed but we have found that this simple independence assumption allows in our case accurate volume reconstruction. Each affine transformations φ_i is composed of a rotation R_i and a translation b_i, *which codes the i^{th} slice position with respect to the frame H_0.* The chosen model is

$$P_{\varphi_i^0}(\varphi_i) \propto \exp(-d^2(\varphi_i,\varphi_i^0)) \ ,$$

where

$$d^2(\varphi_i, \varphi_i^0) = \frac{d^2(R_i, R_i^0)}{\sigma_\omega^2} + \frac{d^2(b_i, b_i^0)}{\sigma_b^2} \,, \tag{7}$$

and σ_ω^2 and σ_b^2 are variance parameters which express how far the affine transformation ϕ is allowed to deviate from the mean position ϕ^0. The distance between two rotations is the common geodesic distance which is invariant to right/left rotation multiplication:

$$d(R, R') = \cos^{-1}\left(\frac{\text{trace}\ (R(R')^{-1}) - \mathbf{1}_{\,m=3}}{2}\right) \,,$$

where m refers to the dimension of rotation matrix (2 or 3). Finally, the distance between two translations is the common Euclidean distance $d^2(b, b') = \|b - b'\|^2_{\mathbb{R}^m}$.

3. Variational formulation

Given the priori and noise models as defined above, the MAP criterion (1) can be expressed as a variational problem for which the solution $(\hat{f}, \hat{\Phi})$ minimizes the energy

$$\begin{aligned}\mathcal{J}(\Phi, f) = \frac{1}{2}\sum_{i=1}^{N} d^2(\varphi_i, \varphi_i^0) + \frac{1}{2\sigma_f^2}\|f\|^2_{\mathcal{H}} \\ + \frac{1}{2}\sum_{i=1}^{N}\sum_{x\in H_0} |f(\varphi_i(x)) - I_i(x)|^2/\sigma_\epsilon^2 \,.\end{aligned} \tag{8}$$

To minimize $\mathcal{J}$, we use a gradient-descent based method defined as

$$\begin{pmatrix}\Phi(t+\delta t)\\ f(t+\delta t)\end{pmatrix} = \begin{pmatrix}\Phi(t)\\ f(t)\end{pmatrix} - \begin{pmatrix}\bigtriangledown_{\Phi(t)}\mathcal{J}\\ \bigtriangledown_{f(t)}\mathcal{J}\end{pmatrix}\delta t \,. \tag{9}$$

We therefore need to express the two partial gradients: $\bigtriangledown_\Phi \mathcal{J}$ and $\bigtriangledown_f \mathcal{J}$.

3.1. Expression for $\bigtriangledown_f \mathcal{J}$

Due to (4), the calculation of $\bigtriangledown_f \mathcal{J}$ can be reduced to a finite dimensional computation. Everything can be expressed in terms of $\alpha \doteq (\alpha_i)_{1\le i\le N_C}$ and the gradient is computed with respect to α, §. We then have

$$\bigtriangledown_\alpha \mathcal{J} = \sigma_f^{-2} K\alpha + A^T(A\alpha - I)/\sigma_\epsilon^2 \,, \tag{10}$$

where

$$\begin{aligned}K &\doteq (k(x_i, x_j))_{1\le i,j\le N_C}\\ A &\doteq (k(\varphi_i(s), x_j))_{1\le i\le N, s\in H_0, 1\le j\le N_C}\\ I &\doteq (I_i(s))_{1\le i\le N, s\in H_0} \,.\end{aligned}$$

§ It is proved in [17] that if the x_i are given as the current positions in space of all the slice pixels, then the optimal solution in f, Φ fixed, can be expressed as (4)

3.2. Expression for $\bigtriangledown_\Phi \mathcal{J}$

The partial gradient $\bigtriangledown_\Phi \mathcal{J}$ is further decomposed into two terms: one for the rotations denoted by $\bigtriangledown_{\mathbf{R}} \mathcal{J}$ (in fact a family $(\bigtriangledown_{R_i} \mathcal{J})_{1 \leq i \leq N}$) and another for the translations denoted by $\bigtriangledown_{\mathbf{b}} \mathcal{J}$ (also a family). It is straightforward to write $\bigtriangledown_{\mathbf{b}} \mathcal{J}$ directly from (8) since it involves only functions based on common Euclidean scalar products. One reads

$$\bigtriangledown_{b_i} \mathcal{J} = \frac{b_i - b^0}{\sigma_b^2} + \sum_{x \in H_0} \frac{(f(\varphi_i(x)) - I_i(x))}{\sigma_\epsilon^2} \bigtriangledown f(\varphi_i(x)) \; . \tag{11}$$

To deduce the partial gradient with respect a rotation R_i, keep in mind that we are computing a derivative on a Lie group and not a vector space. In 2-D, the representation of rotations by their angle allows for a simple derivation. A more sophisticated derivation in the 3-D case is detailed in the following proposition whose proof is given in Appendix.

Proposition : If $R \rightarrow F(R)$ is a smooth valued function defined on 3×3 matrices and $\frac{\partial F}{\partial R} = (\frac{\partial F}{\partial R_{ij}})_{1 \leq i,j \leq 3}$ is the matrix of partial derivatives of F , then its gradient relative to variation *within* the group of rotations $SO(3)$ is

$$\bigtriangledown_R F = \bigtriangledown_R^\omega F \wedge R \tag{12}$$

where $\bigtriangledown_R^\omega F \doteq \frac{1}{2} \sum_{j=1}^3 R_{.j} \wedge (\frac{\partial F}{\partial R})_{.j}$ (operator $()_{.j}$ extracts the matrix's j^{th} column.)

3.3. Optimization procedure

The gradient-descent algorithm (9) alternates between gradient steps on Φ parameters and on α parameters (i.e., the volume f). For a generic slice i, if we omit the index i for sake of simplicity, following (9) and (12), the current rotation matrix value $R(t)$ at time t is updated by

$$R(t + \delta t) = R(t) - (\bigtriangledown_R^\omega \mathcal{J} \wedge R(t)) \, \delta t \; . \tag{13}$$

Because of the presence of δt, we have used the matrix exponential form [27] in order to guarantee that the updated $R(t + \delta t)$ stays in the rotation group without having to make re-orthogonalisation from time to time:

$$R(t + \delta t) = \exp(-[\delta t \bigtriangledown_R^\omega \mathcal{J}]_\times) \, R(t) \; , \tag{14}$$

where $[a]_\times$ denotes the skew-symmetric matrix associated to $(a \wedge .)$. In fact, this formula is a first order Taylor's approximation of (13) obtained from the expansion of the matrix exponential : $\exp(M) \approx I + M$ (I is the identity matrix).

Since the energy term $\mathcal{J}$ w.r.t α is a quadratic term, then from (10) updating α is straightforward. Fixing Φ at $\Phi(t)$ and thus A to $A(t)$, it has an analytical solution:

$$\alpha(t) = (\sigma_f^{-2} \sigma_\epsilon^2 K + A^T A)^{-1} A^T I \; . \tag{15}$$

The positive definite kernel function $k(\cdot, \cdot)$ guarantees the uniqueness of the solution $\alpha(t)$. To overcome the numerical bottleneck in 3-D due to the large value of N_C and the non compact support of Gaussian kernel family, we have implemented a modified Fast Gauss Transform (FGT) algorithm [28] and integrated it in the conjugate gradient method to solve the linear system in (15).

Moreover, updating $\Phi(t)$ involved in (11) and (14) benefits also from the FGT implementation thanks to the close form of $\bigtriangledown_{\Phi(t)}\mathcal{J}$. To speed up the convergence rate of estimating the nonlinear parameters $\Phi(t)$, Levenberg-Marquardt (LM) algorithm [29] is adopted to determine explicitly the step δt. The mixture optimization procedure combining conjugate gradient method and LM algorithm guarantees still its convergence, at least to a local critical point. *With this coordinate-wise procedure the energy term is decreasing at every step except at the end, near the solution, when the gradient becomes too small to be numerically approximated with accuracy. At this point, the process is stopped without loss of accuracy.*

Our current implementation on a standard personal computer (3.6 GHz cpu, 4GB memory and Matlab on Linux environment ‖) requires about one hour per iteration of the optimization procedure (8) for a volume of size 50^3 *from a sequence of* 130 *images of size* 50×50*. Fig. 3 plots the energy curve for 20 iterations. One see that after only 5 iterations the energy level reaches a stable value close to its final convergence value.*

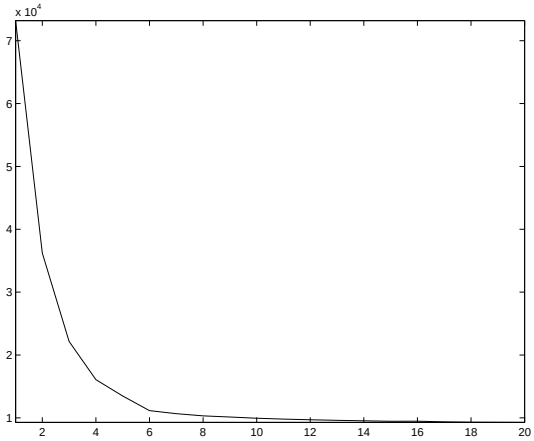

Figure 3. *Energy curve for the reconstruction of a volume of size* 50^3.

4. Parameter calibration

One recurrent hurdle in energy based optimization methods is the proper choice of parameters. The variance parameters σ_b^2 and σ_ω^2 on the initial guesses (see (7)) can be fixed from *p*riori knowledge on their uncertainty. More difficult and crucial is the calibration of the other parameters such as the hyper-parameters σ_ϵ^2, σ_f^2, (see (3) and (6)), which are essential to achieve correct slice positioning and good reconstruction.

We take advantage of our modeling framework to derive a Bayesian estimate of the unknown parameters. In this framework, the priori information is mainly given by the kernel model (5). Indeed, it is well known that this kernel induces a covariance structure on f [22]. For our application, the central point is that, thanks to the rotation and translation invariance

‖ There exists other solutions such as MPI or GPU parallel computation to acceleration of optimization, but they are beyond of the research scope of this paper.

of this covariance structure, for any positioning φ_i of slice i, the vector representation of the slice $F_i \doteq \{f(\varphi_i(x_s))\}_{s\in H_0}$ is a Gaussian vector with covariance matrix *independent* of φ_i:

$$\begin{aligned}\mathrm{cov}(F_i(s), F_i(t)) &= \sigma_f^2 \rho(\|\varphi_i(x_s) - \varphi_i(x_t)\|/\lambda_f) \\ &= \sigma_f^2 \rho(\|x_s - x_t\|/\lambda_f) \ .\end{aligned}$$

Furthermore, we assume that its mean μ_f is constant. Thus under the model assumptions (2), the observed image $I_i = F_i + \epsilon_i$ is a Gaussian vector $\mathcal{N}(\mu_f \mathbb{1}_{H_0}, \Gamma_\theta)$ where the covariance matrix Γ_θ is explicitly given by

$$\Gamma_\theta(s,t) = \sigma_f^2 \rho(\|x_s - x_t\|/\lambda_f) + \sigma_\epsilon^2 \mathbb{1}_{s=t} \ ,$$

where the unknown parameters are now denoted

$$\theta = (\mu_f, \sigma_f^2, \lambda_f, \sigma_\epsilon^2) \ .$$

This brings us to a more classical framework of non linear regression where θ can be chosen in order to optimise the log marginal likelihood of I_i,

$$\log P(I_i|\theta) = \ -\frac{1}{2\sigma_\epsilon^2}(I_i - \mu_f \mathbb{1}_{H_0})^T \Gamma_\theta^{-1} (I_i - \mu_f \mathbb{1}_{H_0}) - \frac{1}{2}\log(|\Gamma_\theta|) + Cte \ .$$

In fact, we use the whole sequence of images, using a conditional independence approximation for the I_i's so that finally

$$\hat{\theta} = \mathrm{argmax}_\theta \sum_{i=1}^{N} \log P(I_i|\theta) \tag{16}$$

By setting $\bigtriangledown_\theta \log P(I_i|\theta) = 0$, it yields:

$$\begin{aligned}&\hat{\mu}_f = (\mathbb{1}^T \Gamma_\theta^{-1} I_i)/(\mathbb{1}^T \Gamma_\theta^{-1} \mathbb{1}) \\ &\hat{\sigma}_\epsilon^2 = \tfrac{1}{N}(I_i - \hat{\mu}_f \mathbb{1})^T \left(\Gamma_\theta/\sigma_\epsilon^2\right)^{-1} (I_i - \hat{\mu}_f \mathbb{1}) \\ &\log P(I_i|\theta) = -\tfrac{1}{2}(N \log \sigma_\epsilon^2 + \textstyle\sum_{i=1}^N \log \gamma_i) + Cte \ .\end{aligned}$$

where eigen-values (γ_i) come from the spectral decomposition of Γ_θ [30] and Cte is a constant. In such a way, there are only two independent parameters: scale factor λ_f and signal-to-noise ratio $\sigma_f^2/\sigma_\epsilon^2$ to be estimated numerically. In order to further reduce the complexity, we split each I_i into a stack of sub-images $\{I_{i,k}\}$ of smaller size and minimize $\sum_{i,k} \log P(I_{i,k}|\theta)$.

5. Experimental Results

Fig.1 describes a simple experiment in two dimensions. Given the 1-D slice sequence whose true positions are depicted in Fig.1(b), alignment and reconstruction have been computed using the technique described above. For the initial position $\Phi(0)$ of the gradient-descent based optimization procedure (9), we have assumed stable rotation and no translation. In Fig.1(d), we see that after five iterations, the estimated positions $\Phi(t)$ converge closely to their ground-truth since the reconstructed object is close to the true object whereas with $\Phi(0)$ the reconstructed object is quite degraded (Fig.1(c)).

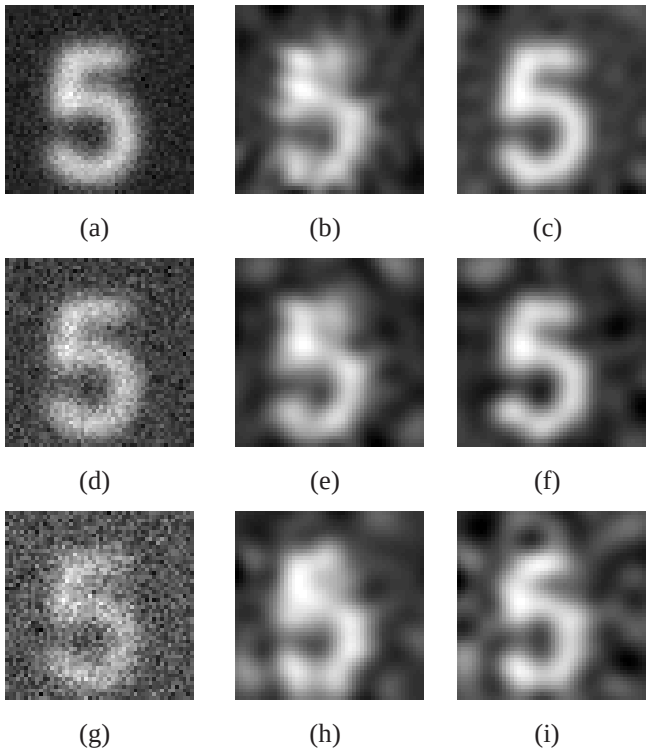

Figure 4. *2-D reconstruction results with different level of noises. For each row, one reads the noisy true image, the reconstructed image without position estimation and the reconstructed image with position estimation. 1D cross-section positions are those shown in Fig. 1(b). The noise levels are : (a)* $\sigma_\epsilon = 0.2\sigma_f$*, (d)* $\sigma_\epsilon = 0.4\sigma_f$*, (g)* $\sigma_\epsilon = 0.75\sigma_f$*.*

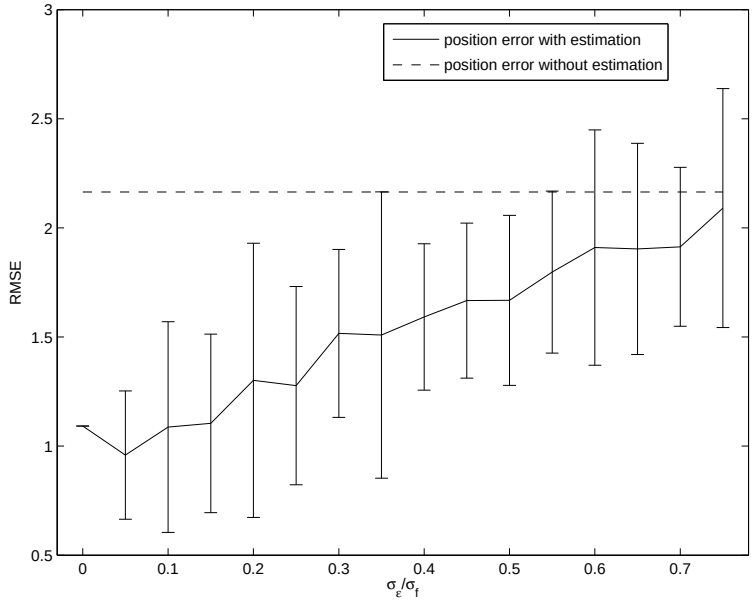

Figure 5. *Empirical curve of the position error and its associated error interval (drawn as 4 times the standard deviation).*

Moreover, an experiment has been done to test the stability of the method with regard to different noise-signal ratios : $\sigma_\epsilon/\sigma_f = 0.2,\ 0.4,\ 0.75$. *On Fig. 4, we see that the quality of the reconstruction is better after alignment than before. However this improvement is reduced when the noise-signal ration becomes too large. In the extreme case the positions are blurred by the noise and are no more perceptible. The noise effect has been analyzed by Monte Carlo computation. For every fixed noise-signal ratio, a sample of 20 different independant realizations of the i.i.d. additive noise are considered. Our procedure was then run on this data set and from the results, the empirical mean of the position error and its standard deviation was computed (see Fig. 5). Since in this simulation test, both the true positions and the initial positions of 1-D slice sequence are fixed, the position error without estimation represented in the dashed line is constant and its value is 2.16 in our case. The RMSE is reduced by a factor 2 for moderate SNR, i.e.,* $\frac{\sigma_\epsilon}{\sigma_f} \leq 0.2$. *Another important remark is that during all the simulation test experiments, the parameters are auto-calibrated exactly by the method described in section 4.*

We describe now a complex experiment in micro-rotation fluorescence microscopy. The real data shown in Fig. 2 (sampling from one tour of 340 slices) was acquired from a living cell cage and suspended in a $Cytocon^{\mathbf{TM}}$ chip (Evotec Technologies, Germany) to investigate the localization and dynamics of nuclear lamina and green fluorescent protein (GFP). ¶

Before launching the reconstruction-alignment coupling processing, the parameters θ needed for the variational formula are estimated by the method proposed in section IV, on 100 blocks of 30×30 uniformly distributed in all 340 slices (the size of each slice is 156×156). The parameters are estimated by MLE criterion as $\sigma_f^2 = 9.75 \times 10^6, \sigma_\epsilon^2 = 3.36 \times 10^5$ and $\lambda_f = 3.5$. The remaining two variance parameters coding the instability of the movement away from the ideal trajectory are set as $\sigma_\omega^2 = 10.0$ and $\sigma_b^2 = 10.0$. *The initialization of the ideal trajectory is determined from the hardware control. Once the cell is trapped inside the dielectrophoretic field cage, the biologist adapts the field in order that the cell undergoes a rotation movement around an ideal fixed axis : ideally an axis within the focal plane. This axis is parameterized and we use it to determine* Φ^0. We have run the optimization procedure determined by (9) for 5 iterations. Each iteration contains a subroutine of volume reconstruction driven by conjugate gradient method with fixed 20 iterations and a subroutine of slices alignment driven by Levenberg-Marquardt method with $20 - 200$ iterations which depends on the distance between the initial and final values of slices positions.

In order to have a fair validation of the reconstruction based on micro-rotation data, we provide also a reconstruction based on the state-of-art z-stack imaging techniques. The z-stack data have been acquired in suspension mode of the $Cytocon^{\mathbf{TM}}$ chip now controlled by a piezo motor to displace the whole cage. With this mode, the slices are parallel and their z-positions are known.$^+$ Here, volume reconstruction is standard. *The slice comparison between*

¶ These confocal images were then collected using a Zeiss $Axiovert^{\mathbf{TM}}$ 200 confocal microscopy. For the optical parameter setting, a 63x water immersion objective is used and numerical aperture (NA) is set to 1.2. Finally, the resolution of each optical section image is 129nm and the chip driver gives us the mean rotation direction projected in 2D optical section (it is y axis or vertical direction in this case study).

$^+$ The step between two planes along z direction is set to 100nm and 181 slices were obtained for the same living

*conventional z-stack and micro-rotation imaging is done by extracting two orthonogal slice pairs using ImageJ's MedNuc OrtView plugin (see Fig. 6). The z-stack was deconvolved whereas the micro-rotation volume was not. In these coronal and sagital views, the nuclear envelope contour from micro-rotation imaging is much better visualized than those from z-stack imaging although micro-rotation volume is not deconvolved (see contours marked by arrows). The small hole in the contour (marked by a rectangle) of the micro-rotation volume is due to the so-called "blind-cone" phenomena : when the rotation axis is not living in the focal plane H_0, the interior of the cone generated by the rotation axis is not sampled during the micro-rotation process. In fact, it can be removed by deconvolution of the reconstructed volume, [**?**] [**?**].* The micro-rotation volume is rendered in the same viewing direction as that the z-stack data (its size is $109 \times 109 \times 181$) which is shown in Fig.7. The positions of each slice coded by rigid transformation parameters are shown in Fig.9, which represents an irregular perturbation in agreement with physical models. This irregular perturbation is apparent on Fig.2, in particular from instant (j) to (k) (upward jump). Note that this jump is well detected on the position parameters in Fig.9.

A deeper biological evaluation is beyond the scope of this paper [**?**]. However, to explain the difference between the two reconstructed volumes, let us give two mains drawbacks of the z-stack mode. First, contrary to the micro-rotation mode, it does not deal with the problem of anisotropy of the microscope resolution: the resolution perpendicular to the focal plane is half of the resolution within the focal plane [31]. Second, it suffers from geometrical distortions : a spherical object does not appear spherical. It is clear from the rendering volume viewing shown in Fig.7 that the reconstruction quality from micro-rotation slices is better than those from deconvoluted z-stack slices: not only it gives the cellular membrane which is missing in the z-stack volume, but also the geometrical distorsion caused by spherical aberration has been reduced.

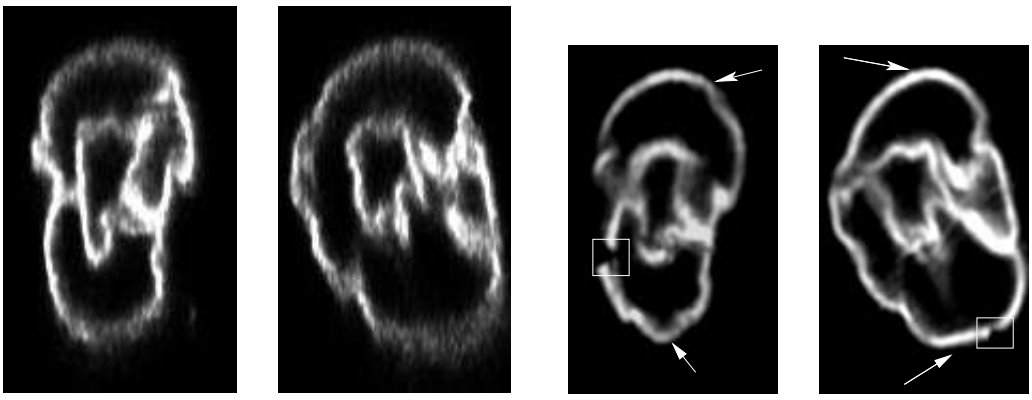

(a) (b) (c) (d)

Figure 6. *Slice comparison between deconvolved z-stack and micro-rotation imaging. (a)-(b) Two orthonogal slices from z-stack deconvolved by SVI Huygens software. (c)-(d) Corresponding orthonogal slices from micro-rotation volume (without deconvolution).*

cell as that used in micro-rotation mode.

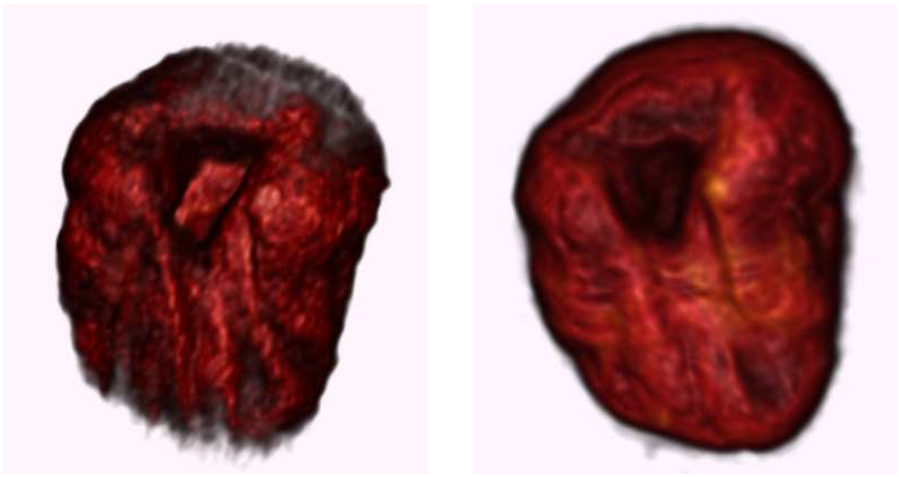

(a) (b)

Figure 7. 3D volume rendering using OsiriX software projected on a same viewing position. (a) From conventional deconvoluted Z stacks. (b) From the micro-rotation volume.

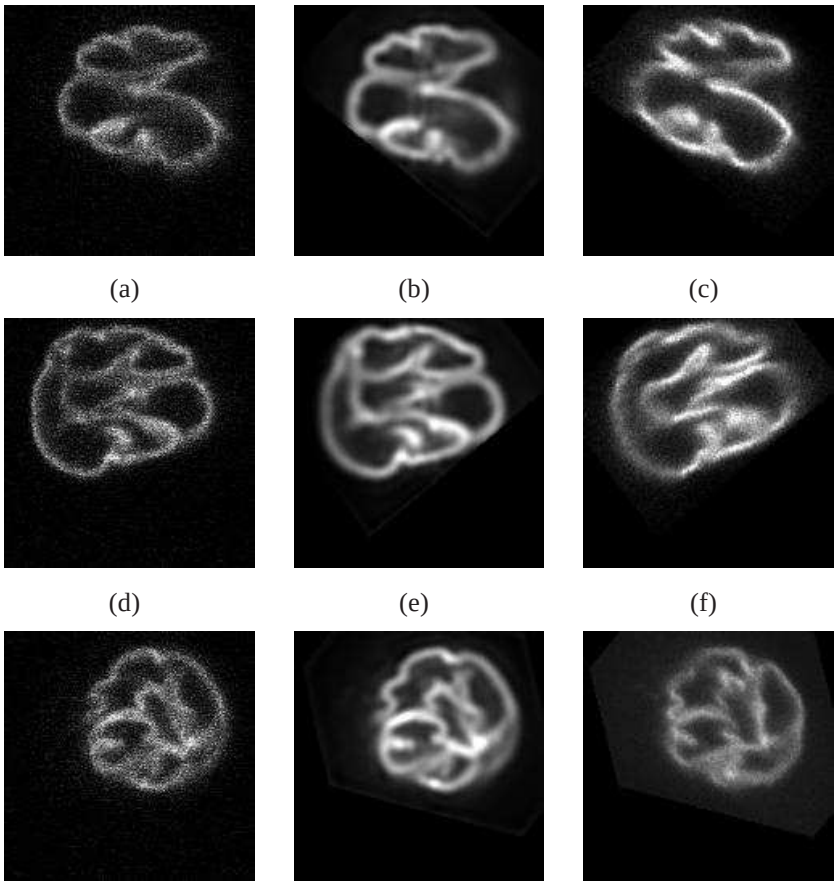

(a) (b) (c)

(d) (e) (f)

(g) (h) (i)

Figure 8. *Slice comparison. Firt column : original slices I_i. Second column : slices interpolated from the reconstruction volume at the estimated position $\hat{\phi}_i$. Third column : slices interpolated from the deconvolved z-stacks at position $\hat{\phi}_i$.*

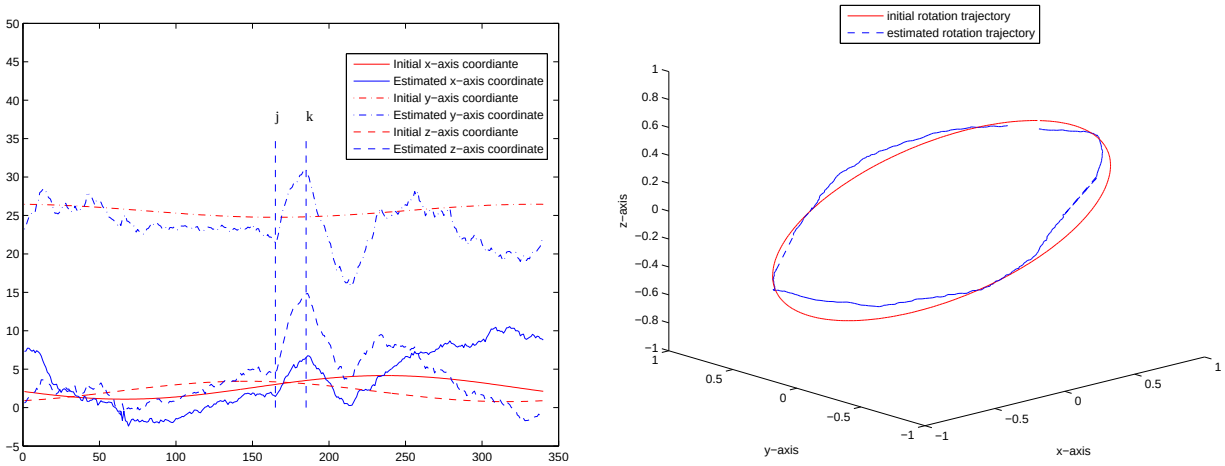

(a) (b)

Figure 9. Rigid transformation estimation of the 340 micro-rotation slices position parameters: (a) translation of each slice (b) trajectory generated from the 340 rotation matrices given by each slice position acting on a unit vector $[1\,0\,0]^t$.

6. Conclusion

In this paper we have demonstrated that it is possible to perform simultaneously alignment and reconstruction. Of crucial importance is the ability to perform parameter calibration in a statistical framework, as well as the explicit modeling of all aspects of uncertainty. It should be emphasized that even with low resolution, the slice positioning parameters can be accurately estimated. The current reconstruction results could be easily improved by a second reconstruction step at high resolution with the slice positions frozen at their estimated values. However, a more principle route to deal with the computational burden of high-resolution is to adopt the multi-resolution strategy. In our case, it consists of representing the volume by a combination of kernels at different scale spaces. Moreover it should be able to avoid local minima during the optimization phase.

7. Appendix

Proof

Lets us start with the derivate of the regular function $F(R)$ defined on the space of 3×3 matrices $\mathcal{M}_3(\mathbb{R})$. Looking R as a function of the time, the derivate at time t_0 is :

$$\frac{d}{dt}F(R(t))_{|t_0} = \langle \frac{\partial F}{\partial R}(R_0), \dot{R}_0 \rangle_{\mathbb{R}^{3\times 3}} , \tag{17}$$

$$\text{where } \dot{R}_0 = \frac{d}{dt}R(t)_{|t_0} .$$

In fact, we have to express this derivative on SO(3) and not simply on $\mathcal{M}_3(\mathbb{R})$.

The derivative $\dot{R}$ of $R(t)$ on $SO(3)$ is well known ([27]). We recall it. By definition, any rotation R satisfies $R^T R = I$. The derivative of this equation yields $\dot{R}R^T = -(\dot{R}R^T)^T$. It follows that $\Omega = \dot{R}R^T$ is a skew symmetric matrix. Such a matrix can be expressed trough a vector $\omega \in \mathbb{R}^3$: $\Omega = [\omega]$ with $[\omega]x = \omega \wedge x$, $\wedge$ denoting the cross product. From $\dot{R}R^T = [\omega]$, we get the result :

$$\dot{R} = [\omega]R \; . \tag{18}$$

At this level, a fundamental remark must be done. Around the identity $R(t) = I$, the first order approximation

$$R(t + dt) \approx R(t) + [\omega]Rdt$$

is simply $R \approx I + [\omega dt]$. So, vector space so(3)=$\{[\omega],\ \omega \in \mathbb{R}^3\}$ is called the tangent space at the identity to SO(3). If $R(t)$ is not the identity, the tangent space is so(3) transported by R, that is : $\mathbf{T}_R(SO(3)) = \{[\omega]R,\ \omega \in \mathbb{R}^3\}$.

Let us come to the gradient of F within SO(3). Now, we know that $\dot{R}$ as defined in (18) belongs to $\mathbf{T}_R(SO(3))$. With this constraint, the scalar product in (17) can be written

$$\langle \frac{\partial F}{\partial R}, \dot{R} \rangle_{\mathbb{R}^{3\times 3}} = \langle \mathcal{P}\frac{\partial F}{\partial R}, \dot{R} \rangle_{\mathbb{R}^{3\times 3}} \; , \tag{19}$$

where $\mathcal{P}$ is the projection on $\mathbf{T}_R(SO(3))$. Denote $\bigtriangledown_R F = \mathcal{P}\frac{\partial F}{\partial R}$. Since $\bigtriangledown_R F$ belongs to $\mathbf{T}_R(SO(3))$, it exists a vector $\hat{\omega} \in \mathbb{R}^3$ such that

$$\bigtriangledown_R F = [\hat{\omega}]R \; . \tag{20}$$

It implies the following development of the right side of (19) :

$$\begin{aligned} \langle \bigtriangledown_R F, \dot{R} \rangle_{\mathbb{R}^{3\times 3}} &= \langle [\hat{\omega}]R, [\omega]R \rangle_{\mathbb{R}^{3\times 3}} \\ &= 2\langle \hat{\omega}, \omega \rangle_{\mathbb{R}^3} \; . \end{aligned} \tag{21}$$

On other hand, using the property $\langle a, b \wedge c \rangle = \langle c \wedge a, b \rangle$, the left side of (19) becomes

$$\begin{aligned} \langle \frac{\partial F}{\partial R}, [\omega]R \rangle_{\mathbb{R}^{3\times 3}} &= \sum_{j=1}^{3} \langle \left(\frac{\partial F}{\partial R}\right)_{.j}, \omega \wedge R_{.j} \rangle_{\mathbb{R}^3} \\ &= \langle \sum_{j=1}^{3} R_{.j} \wedge \left(\frac{\partial F}{\partial R}\right)_{.j}, \omega \rangle_{\mathbb{R}^3} \; . \end{aligned} \tag{22}$$

Thus, identifying (21) and (22) , we find

$$\hat{\omega} = \frac{1}{2}\sum_{j=1}^{3} R_{.j} \wedge \left(\frac{\partial F}{\partial R}\right)_{.j} \; ,$$

and recalling 20 we get the final result $\bigtriangledown_R F = \hat{\omega} \wedge R$.

8. Acknowledgements

This research is supported by the French Ministry of Research (grant ACI-NIM FLUTOMY 2003 and Postdoctoral Fellowship 2004) and by the European Commission (NEST 2005

Programme) in consortium AUTOMATION, coordinated by S.L. Shorte (Institut Pasteur, http://www. pfid.org/AUTO MATION/ home/). We would like to thank the anonymous referees for their comments which help us a lot to clarify the first version of this paper.

References

[1] Y. Yu, A. Trouvé, and B. Chalmond. A bayesian 3d volume reconstruction for confocal micro-rotation cell imaging. In A. Maeder N. Ayache, S. Ourselin, editor, *MICCAI 2007*, volume II, pages 685–692. Springer-Verlag Berlin Heidelberg, 2007.

[2] O. Renaud, J. Vina, Y. Yu, C. Machu, H. Van der Voort A. Trouvé, B. Chalmond, and S. L. Shorte. High-resolution imaging of living cells in flow suspension using axial-tomography: 3d imaging flow cytometry. Biotechnology Journal, to appear, 2007.

[3] J. Bradl, B. Rinke, B. Schneider, P. Edelman, M. Hausmann, and C. Cremer. Resolution improvement in 3-d microscopy by object tilting. *Microsc. Anal.*, 44:9–11, 1996.

[4] C. J. Cogswell, K. G. Larkin, and H. U. Klemm. Fluorescence micro-tomography: multi-angle image acquisition and 3d reconstruction. In *Proc. SPIE*, volume 2655, 1996.

[5] R. Heintzmann and C. Cremer. Axial tomographic confocal fluorescence microscopy. *Journal of Microscopy*, 206:7–23, 2002.

[6] S. Kawata. The optical computed tomography microscope. *Advance. Opt. Electron. Microsc.*, 14:213–248, 1994.

[7] J. Sharpe, U. Ahlgren, P. Perry, B. Hill, A. Ross, J. Hecksher-Sorensen, R. Baldock, and D. Davidson. Optical projection tomography as tool for 3d microscopy and gene expression studies. *Science*, 296:541–545, 2002.

[8] P.J. Shaw, D.A. Agard, Y. Hiraoka, and J.W. Sedat. Tilted view reconstruction in optical microscopy: Three-dimensional reconstruction of drosophila melanogaster embryo nuclei. *Biophysical journal*, 55:101–110, 1989.

[9] T. Schnelle, R. Hagedorm, G. Fuhr, S. Fielder, and T. Muller. Three-dimensional electric field traps for manipulation of cells - calculation and experimental verification. *Biochemica et Biophysica Acta*, 1157:127–140, 1993.

[10] N.A. Woods, N.P. Galatsanos, and A.K. Katsaggelos. Em-based simultaneous registration, restoration, and interpolation of super-resolved images. In *IEEE ICIP*, 2003.

[11] A. Chiuso, R. Brocket, and S. Soatto. Optimal structure from motion: Local ambiguities and global estimates. In *IEEE CVPR*, 1998.

[12] Samit Basu and Yoram Bresler. Uniqueness of tomography with unknown view angles. *IEEE Transactions on Image Processing*, 9(6):1094–1106, 2000.

[13] Samit Basu and Yoram Bresler. Feasibility of tomography with unknown view angles. *IEEE Transactions on Image Processing*, 9(6):1107–1122, 2000.

[14] D. Salzman. A method of general moments for orienting 2d projections of unkown 3d objects. *CVGIP*, 50:129–156, 1990.

[15] Pawel A. Penczek, Jun Zhu, and Joachim Frank. A common-lines based method for determining orientations for $n > 3$ particle projections simultaneously. *ultramicroscopy*, (3-4):205–218, 1996.

[16] P. D. Lauren and N. Nandhakumar. Estimating the viewing parameters of random, noisy projections of asymmetric objects for tomographic reconstruction. *IEEE Trans. Patt. Analy. Mach. Init.*, 19:417–430, May 1997.

[17] G. Matheron. Splines and kriging: their formal equivalence. In Merriam D.F., editor, *Down-to-Earth Statistics: Solutions Looking for Geological Problems*, pages 77–95, 1981.

[18] M. Unser. Sampling-50 years after shannon. *Proceedings of the IEEE*, 88(4):569–587, 2000.

[19] B. Chalmond. *Modelling and inverse problems in image analysis*. Springer-Verlag, New-York, 2003.

[20] N. A. Cressie. *Statistics for spatial data*. Wiley-Intersciences, New York, 1993.

[21] J. T. Kent and K. V. Mardia. The link between kriging and thin plates. In F. P. Keller, editor, *Probability, Statistics and Optimization*. John-Wiley, 1994.

[22] G. Wahba. *Advances in Kernel Methods*, chapter Support vector machines, reproducing kernel Hilbert spaces and the randomized GACV, pages 69–88. MIT Press, 1999.

[23] J. B. T. M. Roerdink. Computerized tomography and its applications: a guided tour. *Niew Archief voor Wiskunde*, 10(3):277–308, 1992.

[24] Sami Sebastian Brandt and Ville Kolehmainen. Structure-from-motion without correspondence from tomographic projections by bayesian inversion theory. *IEEE Trans. on medical imaing*, 26(2):417–430, Februray 2007.

[25] B. Chalmond, F. Coldefy, and B. Laveyssiére. Tomographic reconstruction from non-calibrated nosiy projections in non-destructive evaluation. *Inverse problem*, 15:339–411, 1999.

[26] S. Geman and D. E. McLure. Bayesian image analysis: An application to single photon emission tomography. In American Statistical Society, editor, *Proc. of the Statistical Computing Section*, pages 12–23, 1985.

[27] Y. Ma, S. Soatto, J. Kosecka Shankar, and S. Sastry. *An invitation to 3-D vision from images to geometric models*. Springer, 2004.

[28] C. Yang, R. Duraiswami, N. Gumerov, and L. Davis. Improved fast gauss transform and efficient kernel density estimation. In *IEEE ICCV*, pages 464–471, 2003.

[29] D. Marquardt. An algorithm for least-squares estimation of nonlinear parameters. *SIAM J. Appl. Math.*, 11:431–441, 1963.

[30] G. H. Golub and C. F. Van Loan. *Matrix computations*. Johns Hopkins University Press, 1989.

[31] S.L. Shorte and S. Bolsover. *Florescent and Luminescent Probes*, chapter Imaging reality: Understanding maps of physiology cell signals measured by fluorescence microscopy and digital imaging, pages 94–106. Academic Press, 2nd ed. edition, 1999.